Supporting Information

For

Rice-like and rose-like zinc silicates anchored on amorphous carbon derived from natural reed leaves for high-performance supercapacitors

Shaoqing Zhang [a,*], Yanyan Liu [b], Jiqi Zheng [c, d], Yang Mu [b], Hanmei Jiang [b], Haoran Yan [a], Yanping Wang [a], Yifu Zhang [b], Changgong Meng [b,*]

[a] College of chemistry and materials engineering, Anhui Science and Technology University, Bengbu 239000, China

[b] School of chemical engineering, Dalian University of Technology, Dalian 116024, China

[c] College of environment and chemical engineering, Dalian University, Dalian 116622, China

[d] Department of materials science and engineering, University of Washington, Seattle, WA 98125, USA

* Corresponding author. E-mail address: zhangsq@ahstu.edu.cn (S. Zhang); cgmeng@dlut.edu.cn (C. Meng)

2.1 Material characterizations

X-ray diffraction (XRD) was used to identify the compositions and structures of the products using Bruker D8 Discover X-ray diffractometer with an ImS 2-D detection system (50 kV, 1000 mA). Raman spectra were recorded on a Renishaw InVia Raman microscope with a laser excitation sources of 532 nm. Fourier transform infrared spectroscopy (FTIR) spectra were collected on a Nicolet 6700 spectrometer from 4000 to 400 cm^{-1} using the KBr pellet technique. X-ray photoelectron spectrum (XPS) was taken on a Thermo ESCALAB 250XiX spectrometer with monochromatized Al Kα X-ray (hν = 1486.6 eV). Inductively Coupled Plasma (ICP, PerkinElmer, Optima 2000DV) was adopted to analyze the content of metal elements. A linear relationship was assumed between the edge position and oxidation state. The microstructures and chemical compositions of the products were characterized by a field-emission scanning electron microscope (FE-SEM, FEI Sirion) with an Energy-dispersive X-ray spectrometer (EDS) and transmission electron microscopy (JEOL-JEM2100F). The Brunauer-Emmet-Teller (BET) surface areas of the samples were determined by a Micromeritics ASAP-2020 porosity analyzer after being degassed at 150 ℃ for 10 h.

2.2 Electrochemical characterizations

The working electrodes were prepared by mixing active materials, carbon black and polyvinylidenedifluoride (PVDF) together in a weight of 8:1:1. Then a small quantity of N-methyl-2-pyrrolidone (NMP) was dropwise added into the mixture to dissolve it homogeneously. The mixed slurry was then coated onto a nickel foam with an area of 1×1 cm^2 and dried at 100 °C for 24 h to remove organic solvent, then pressed under a pressure of 10 MPa for 10 min to obtain the working electrode. The mass loading of active materials on the nickel foam was typically 3-4 mg cm^{-2}. Electrochemical characterization was carried out in a three-electrode system in 3 $mol \cdot L^{-1}$ KOH aqueous solution, where Hg/HgO and carbon rod were regarded as the reference electrode and the counter electrode, respectively. The flexible solid-state asymmetric supercapacitors (ASCs)

were constructed from working electrode and activated carbon (AC) electrode using a membrane filter (NKK-PF30AC) as a separator. The ASCs denoted as C-ZnSi-N_2//AC and C-ZnSi-CO_2//AC. Both of the electrodes were prepared in the same way as that used for the preparation of the working electrode in the three-electrode system. For the purpose of getting a better performance of the device, the mass ratio of the positive to negative electrode is balanced on the basis of the equal charge between cathode and anode. The electrolyte was used 3 mol·L^{-1} polyvinyl alcohol/KOH (PVA/KOH) gel electrolyte. After dipping in the electrolyte, the entire device was sealed in plastic sheet to avoid the evaporation of electrolyte. The electrochemical characteristics of the ASCs devices were evaluated by galvanostatic charge-discharge (GCD), cyclic voltammetry (CV) and electrochemical impedance spectroscopy (EIS) measurements. The contribution of the nickel foam to the capacitance can be negligible [1]. The specific capacitance (C) of a single electrode was calculated on the basis of GCD according to the equation (1-2):

$$Cs = \frac{I \cdot \Delta t}{s \cdot \Delta V} \quad (1)$$

$$C = \frac{I \cdot \Delta t}{m \cdot \Delta V} \quad (2)$$

Where Cs (mF cm^{-2}) and C (F g^{-1}) represent areal and specific capacitance, respectively; I (A) denotes discharge current; Δt (s) signifies discharge time; s (cm^{-2}) corresponds to the area of working electrode; m (g) corresponds to the mass of the active material in the working electrode, and ΔV (V) refers to the potential window. The areal capacitance, areal capacity, energy density and power density of the ASC device were calculated on the basis of the equations (3-4):

$$E = \frac{1}{2} Cs \cdot (\Delta V)^2 \quad (3)$$

$$P = \frac{E}{\Delta t} \quad (4)$$

Where E (Wh·m^{-2}) is the energy density and P (W·m^{-2}) is the power density, respectively.

Figure S1

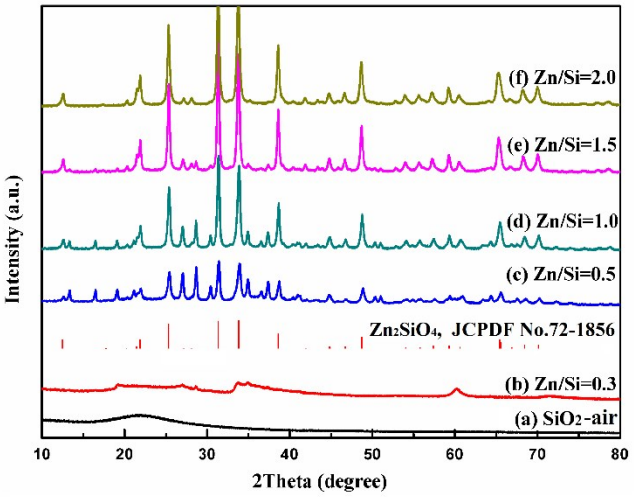

Fig. S1. XRD patterns of the products synthesized with various ratios of Zn/Si by SiO_2-air.

Figure S2

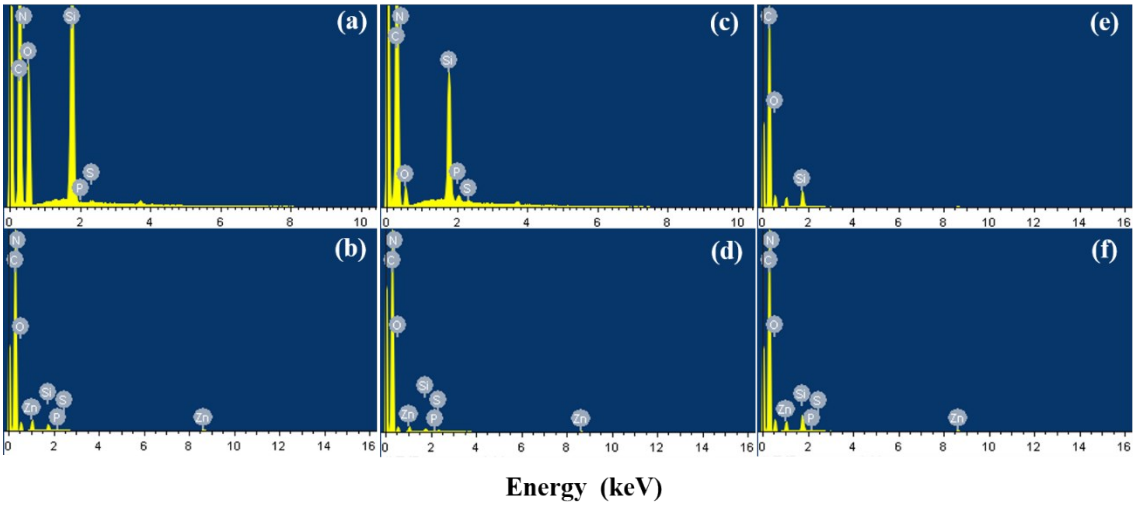

Fig. S2. EDS spectra of (a) C-SiO_2-air, (b) C-ZnSi-air, (c) C-SiO_2-N_2, (d) C-ZnSi-N_2, (e) C-SiO_2-CO_2 and (f) C-ZnSi-CO_2.

Figure S3

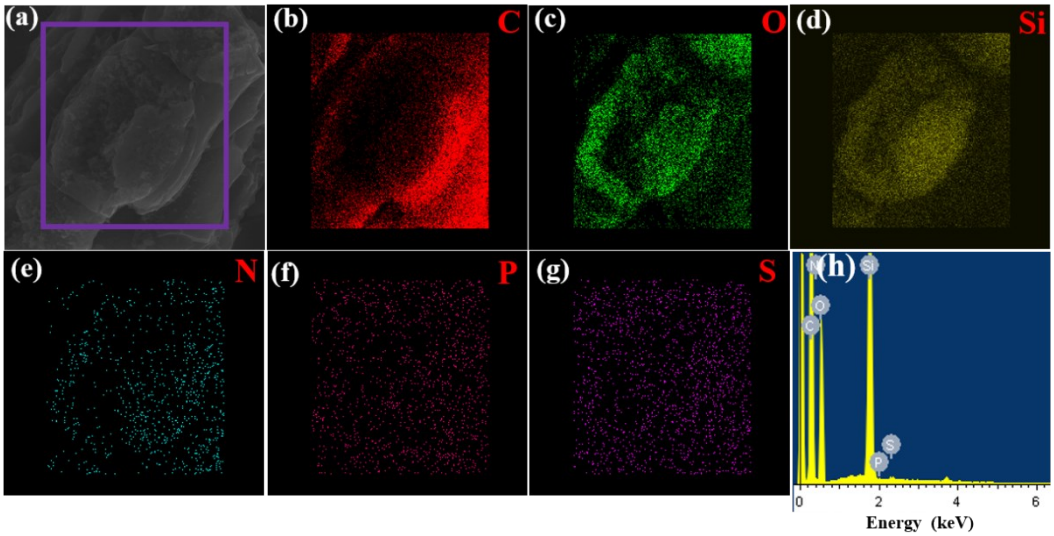

Fig. S3. Elemental mapping images of C-SiO_2-N_2: (a) SEM image, (b) C-K, (c) O-K, (d) Si-K, (e) N-K, (f) P-K, (g) S-K, and (h) EDS of C-SiO_2-N_2.

Figure S4

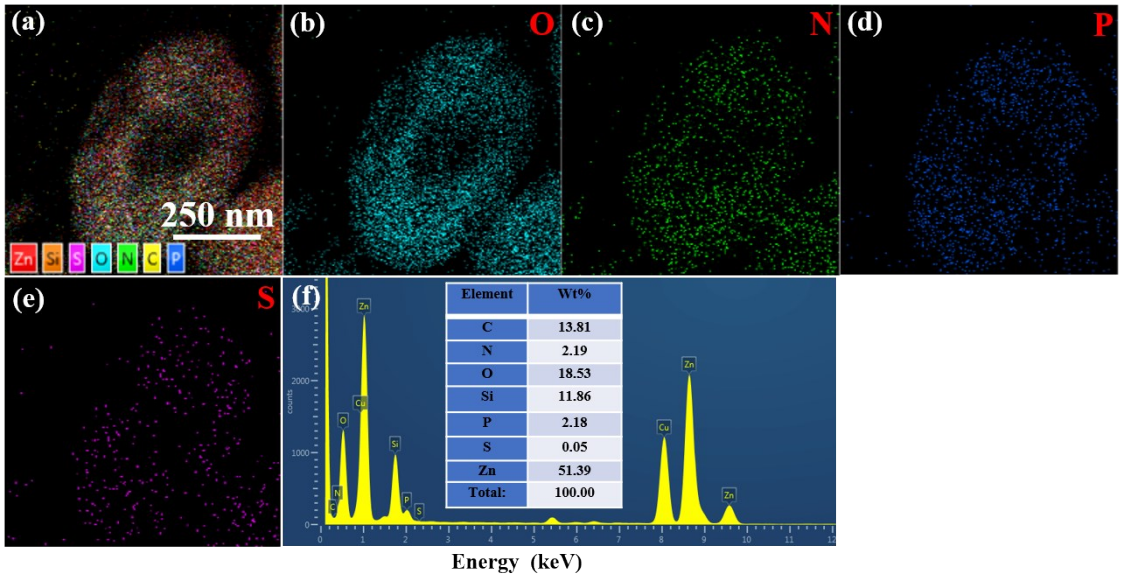

Fig. S4. Elemental mapping images by TEM of C-ZnSi-N_2: (a) EDS layered image, (b) O-K, (c) N-K, (d) P-K, (e) S-K, and (f) EDS of C-ZnSi-N_2. C-ZnSi-N_2 shows a morphology of rice-like microspheres, and all elements have homogeneous distributions.

Figure S5

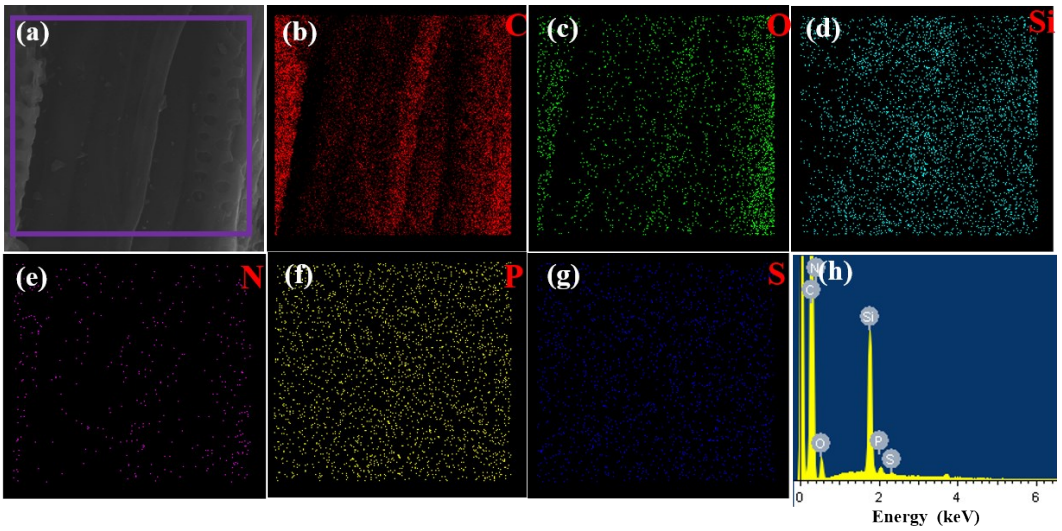

Fig. S5. Elemental mapping images of C-SiO_2-CO_2: (a) SEM image, (b) C-K, (c) O-K, (d) Si-K, (e) N-K, (f) P-K, (g) S-K, and (h) EDS of C-SiO_2-CO_2.

Figure S6

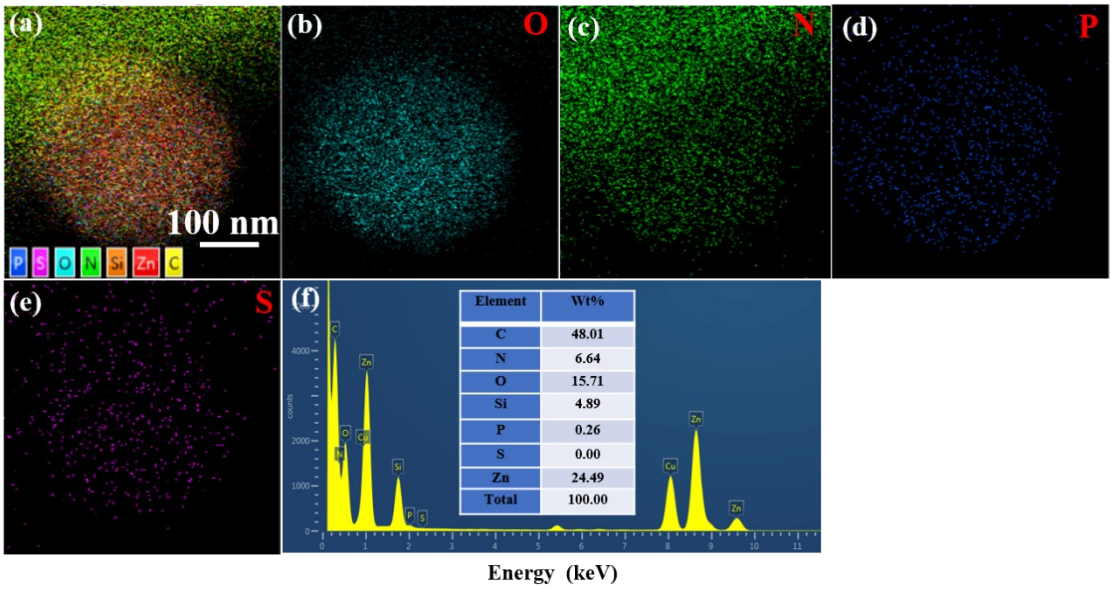

Fig. S6. Elemental mapping images of C-ZnSi-CO_2 by TEM: (a) EDS layered image, (b) O-K, (c) N-K, (d) P-K, (e) S-K, and (f) EDS of C-ZnSi-CO_2. C-ZnSi-CO_2 shows a morphology of rice-like microspheres, and all elements have homogeneous distributions.

Figure S7

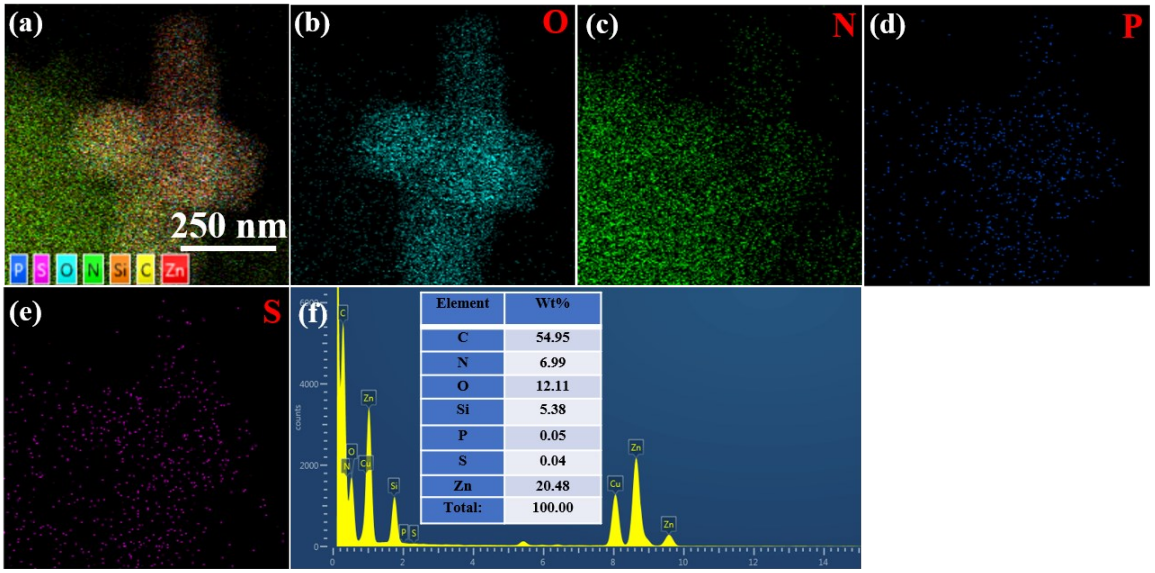

Fig. S7. Elemental mapping images of C-ZnSi-CO_2 by TEM: (a) EDS layered image, (b) O-K, (c) N-K, (d) P-K, (e) S-K, and (f) EDS of C-ZnSi-CO_2. C-ZnSi-CO_2 shows a morphology of rose-like microspheres, and all elements have homogeneous distributions.

Figure S8

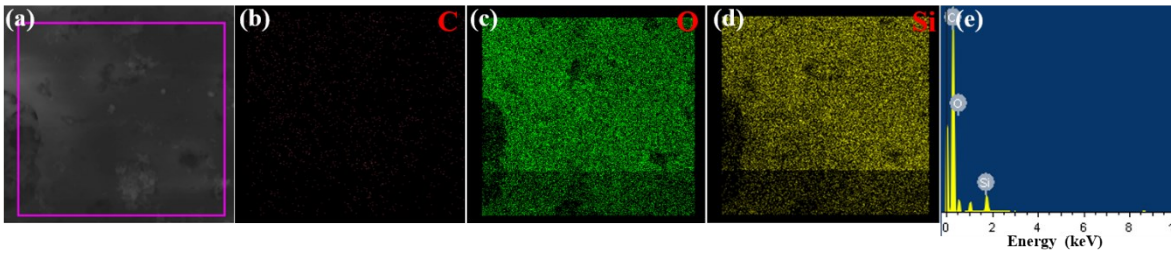

Fig. S8. Elemental mapping images of SiO_2-air: (a) SEM image, (b) C-K, (c) O-K, (d) Si-K, and (e) EDS of SiO_2-air.

Figure S9

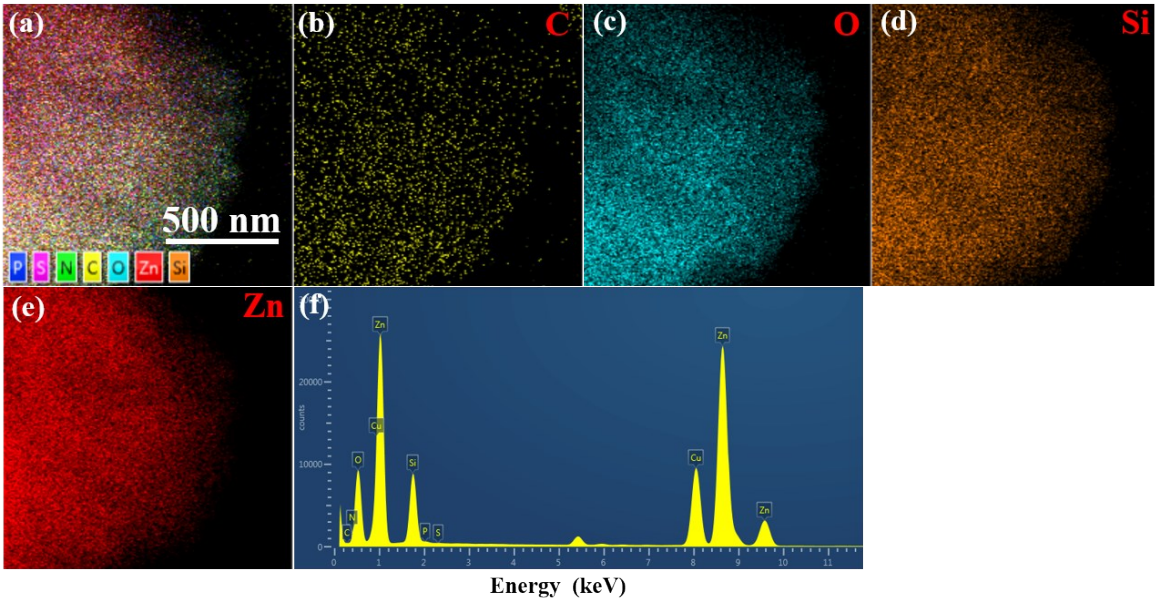

Fig. S9. Elemental mapping images of ZnSi-air by TEM: (a) EDS layered image, (b) C-K, (c) O-K, (d) Si-K, (e) N-K, (f) P-K, (g) S-K, (h) Zn-K, and (i) EDS of ZnSi-air.

Figure S10

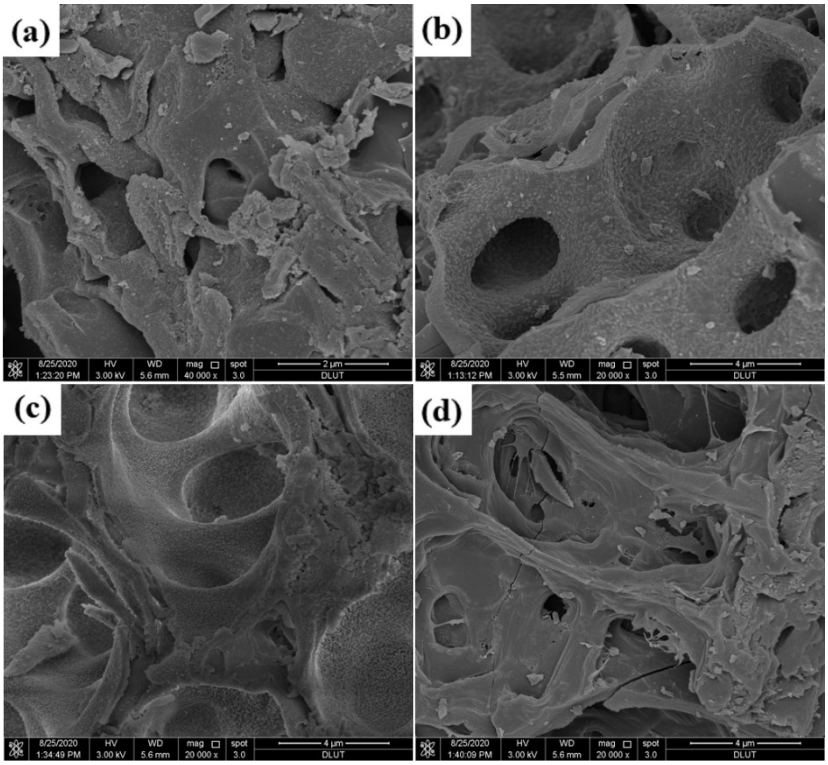

Fig. S10. FE-SEM images of (a) C-SiO_2-N_2, (b) C-SiO_2-CO_2, (c) SiO_2-air and (d) ZnSi-air.

Figure S11

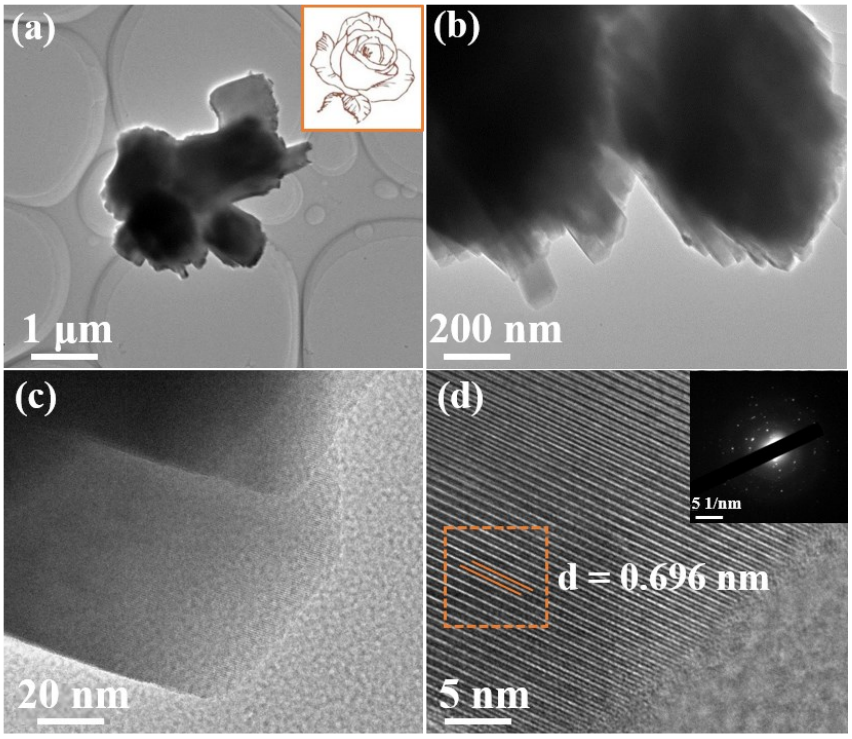

Fig. S11. TEM images (a-b) and the HRTEM image (c-d) of ZnSi-air. ZnSi-air shows a morphology of rose-like microspheres.

Figure S12

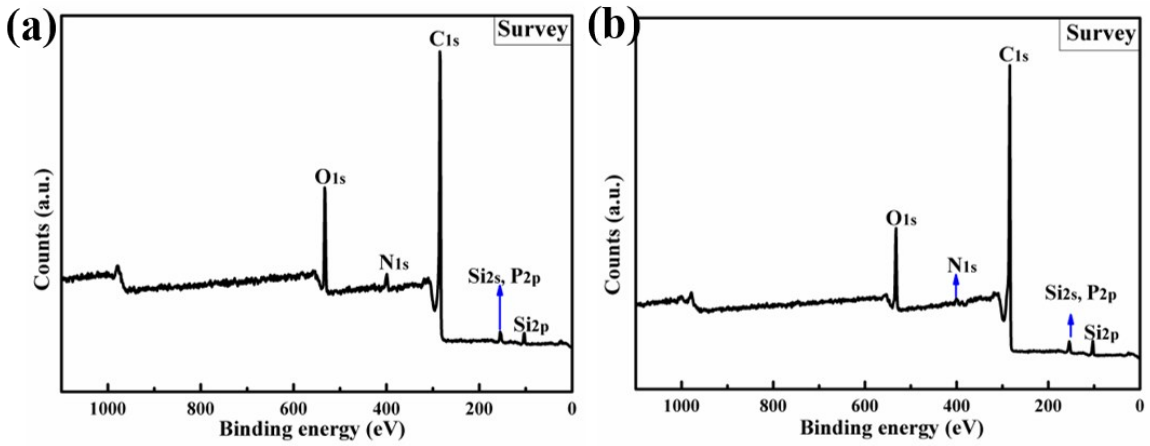

Fig. S12. Survey XPS spectra of C-SiO_2-N_2 (a) and C-SiO_2-CO_2 (b).

Figure S13

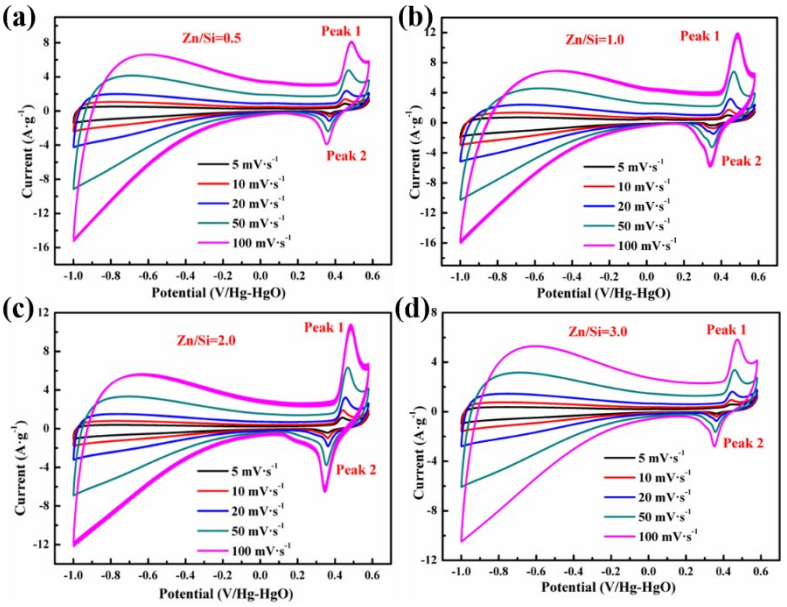

Fig. S13. CV curves of the C-ZnSi-N_2 composites with various ratios of Zn/Si at different scan rates from 5 mV s^{-1} to 100 mV s^{-1}.

Figure S14

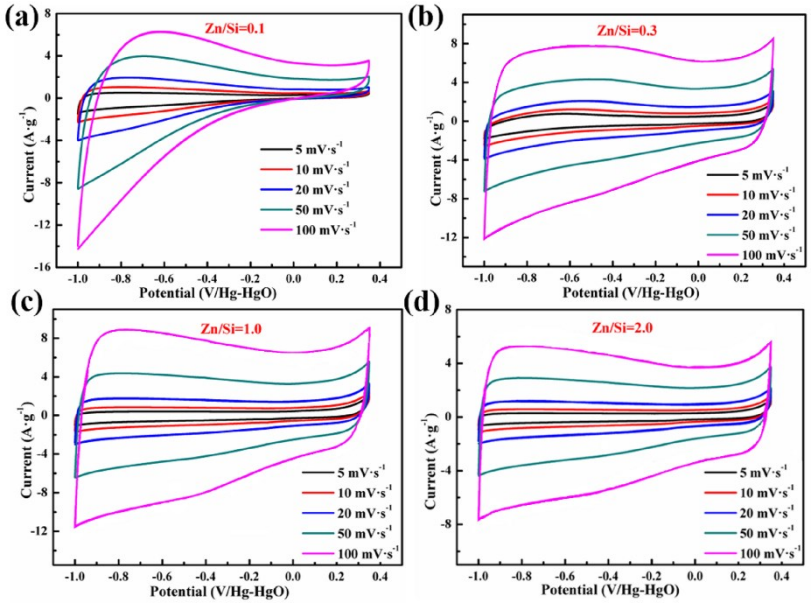

Fig. S14. CV curves of the C-ZnSi-CO_2 composites with various ratios of Zn/Si at different scan rates from 5 mV s^{-1} to 100 mV s^{-1}.

Figure S15

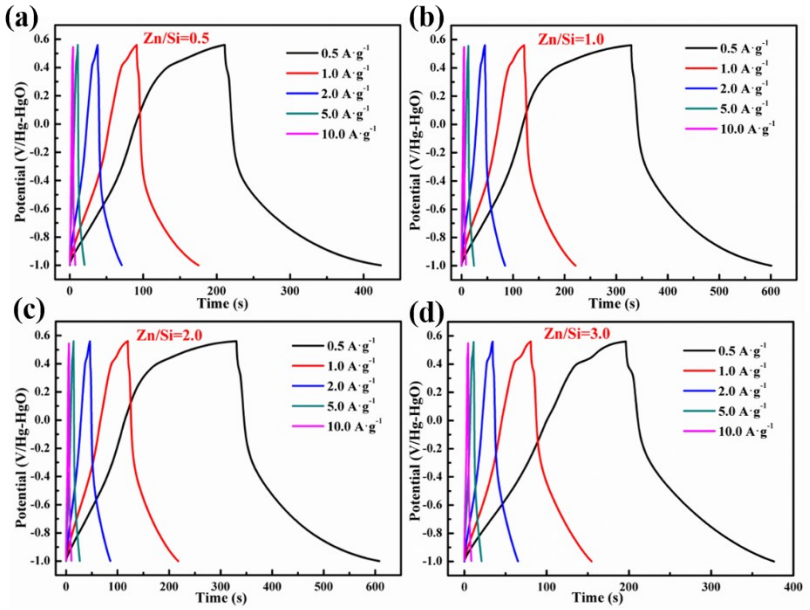

Fig. S15. GCD curves of the C-ZnSi-N_2 composites with various ratios of Zn/Si at different current densities from 0.5 mA cm^{-2} to 10 mA cm^{-2}.

Figure S16

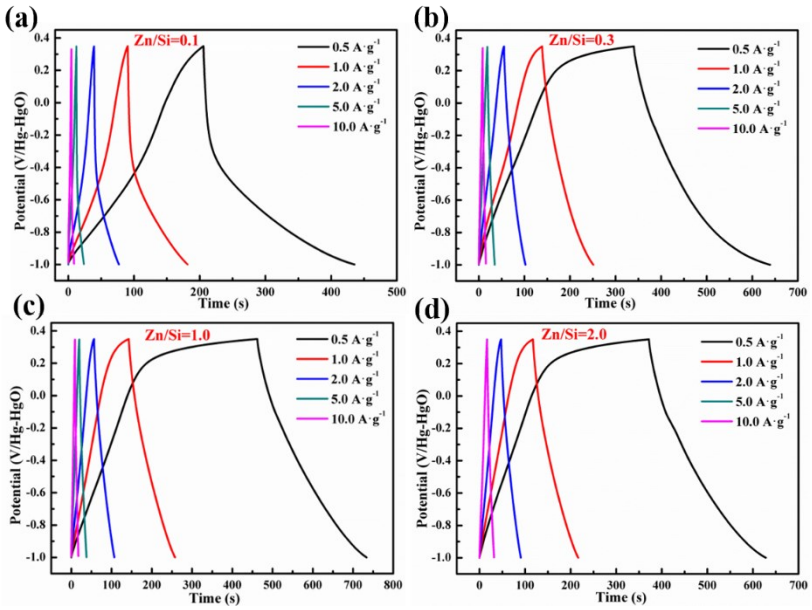

Fig. S16. GCD curves of the C-ZnSi-CO_2 composites with various ratios of Zn/Si at different current densities from 0.5 mA cm^{-2} to 10 mA cm^{-2}.

Figure S17

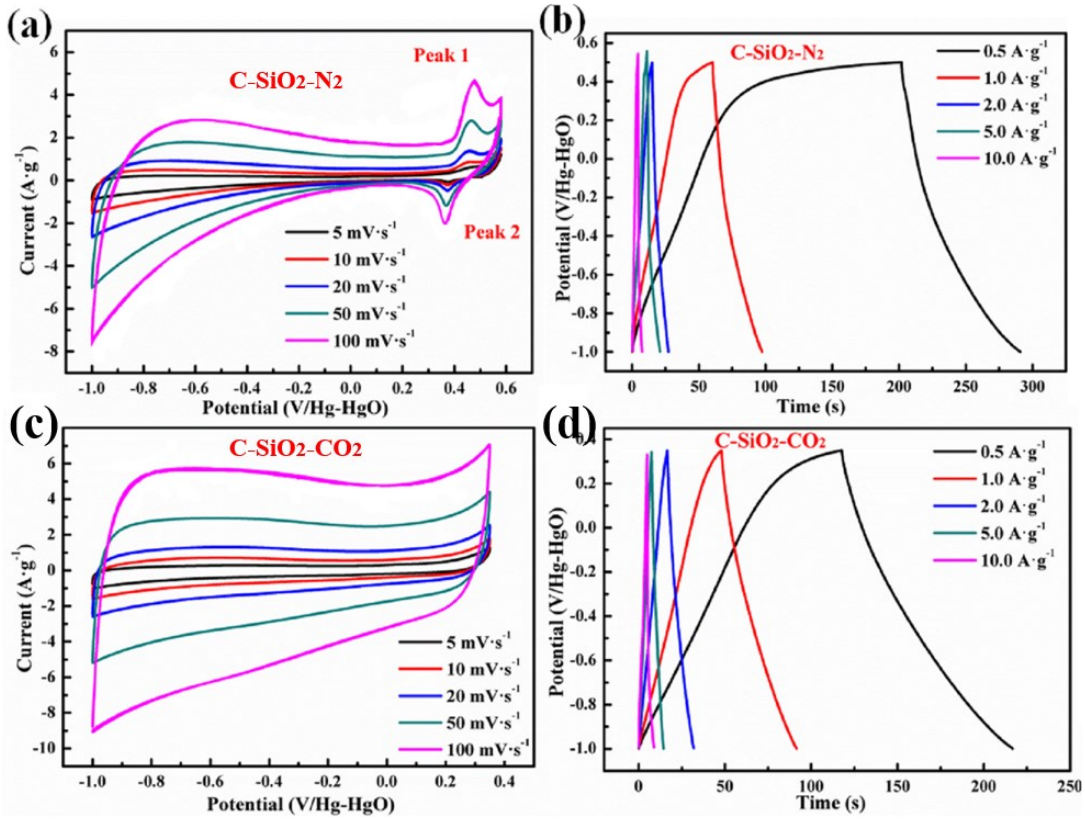

Fig. S17. Electrochemical properties of C-SiO_2-N_2 and C-SiO_2-CO_2 composites: (a) CV and (b) GCD curves of C-SiO_2-N_2 at various ratios of Zn/Si; (c) CV and (d) GCD curves of C-SiO_2-CO_2 at various ratios of Zn/Si.

Figure S18

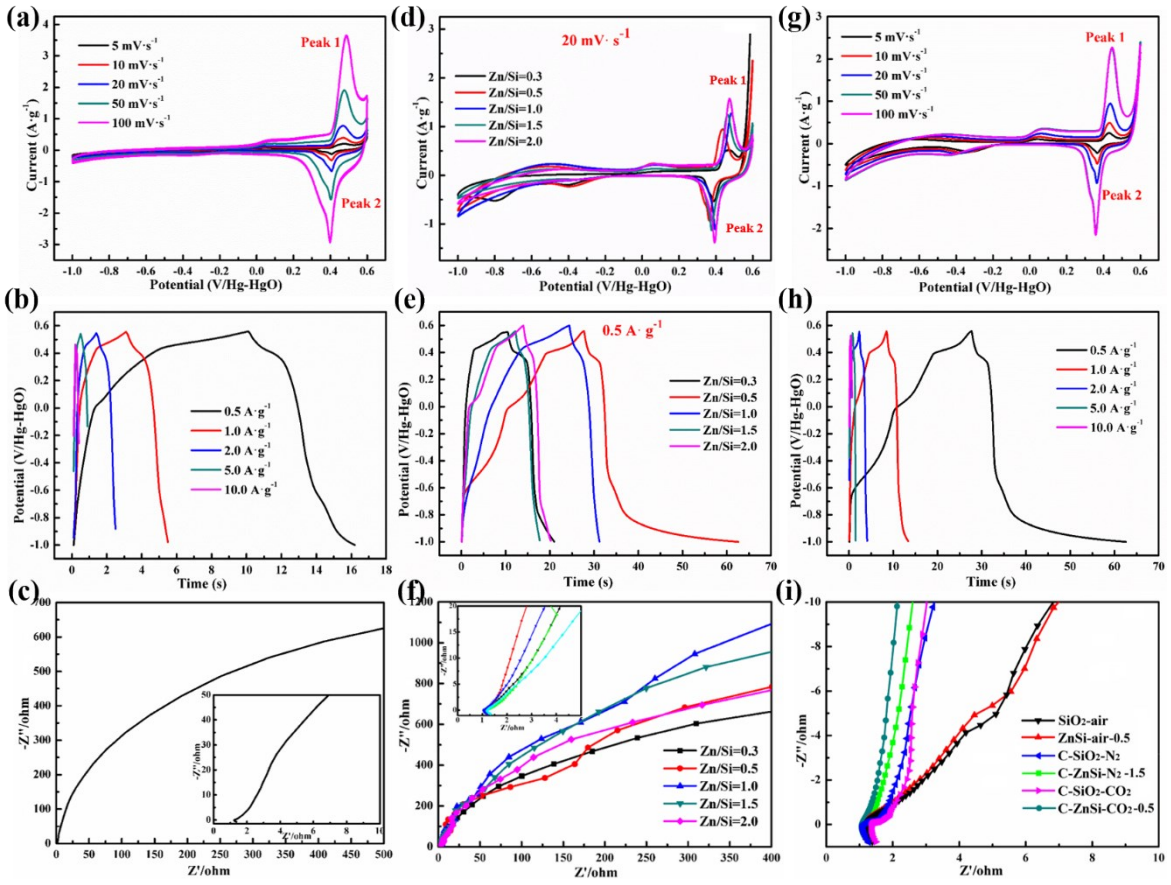

Fig. S18. Electrochemical properties of SiO_2-air and ZnSi-air composites: (a) CV, (b) GCD and (c) Nyquist plot curves of SiO_2-air; (d) CV, (e) GCD and (f) Nyquist plots curves of ZnSi-air at various ratios of Zn/Si; (g) CV and (h) GCD of ZnSi-air-0.5 at different scan rates (from 5 to 100 mV s^{-1}) and current densities (from 0.5 to 10 A g^{-1}), respectively; (i) Nyquist plots curves of SiO_2-air, ZnSi-air-0.5, C-SiO_2-N_2, C-ZnSi-N_2-1.5, C-SiO_2-CO_2 and C-ZnSi-CO_2-0.5.

Figure S19

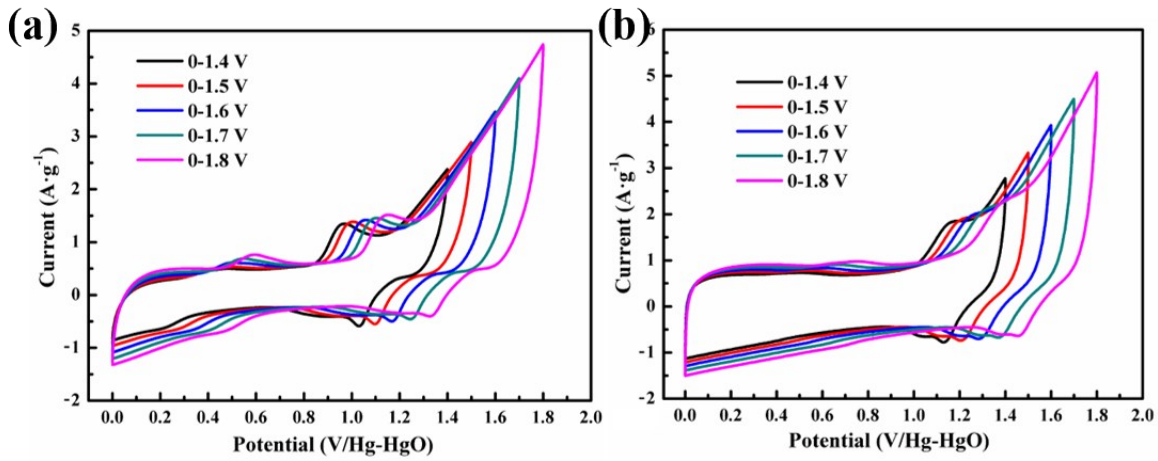

Fig. S19. CV curves of C-ZnSi-N_2//AC (a) and C-ZnSi-CO_2//AC (b) supercapacitors at the scan of 20 mV s^{-1} on various potential limits.

Table S1. Pore Parameters of C-SiO_2-N_2, C-ZnSi-N_2, C-SiO_2-CO_2 and C-ZnSi-CO_2.

sample	BET surface area (m^2 g^{-1})	total pore vol (cm^3 g^{-1})
C-SiO_2-N_2	418	0.389
C-ZnSi-N_2	601	0.537
C-SiO_2-CO_2	391	0.403
C-ZnSi-CO_2	569	0.521

Table S2. Comparison of the specific capacitance of the N, S, P-doped C-$Zn_4Si_2O_7(OH)_2 \cdot H_2O$, C-$Zn_2SiO_4$ and the previously reported Si- and Zn-based materials.

Si- or Zn-based materials	Electrolyte [a]	Potential /V	Capacitance/mF cm^{-2}	Cycling capability	Reference
$Ni_3Si_2O_5(OH)_4$/RGO	2 M KOH	0.2 ~ 0.6	178.9 F g^{-1}, 1 A g^{-1}	97.6 % after 5000	[2]
$MnSiO_3$	6 M KOH	0.2~0.6	251 F·g^{-1}, 0.6 A·g^{-1}	—	[3]
Manganese silicate drapes	1 M KOH	-0.5 ~ 0.4	283 F g^{-1}, 0.5 A g^{-1}	74.7 % after 1000	[4]
$(Ni, Co)_3Si_2O_5(OH)_4$	1 M KOH	0 ~ 0.5	144 F g^{-1}, 1 A g^{-1}	99.3 % after 10000	[5]
Mesoporous-Li_2MnSiO_4	2 M KOH	0 ~ 0.55	120 F g^{-1}, 20 mV·s^{-1}	85.7 % after 500	[6]
$Ni_3Si_2O_5(OH)_4$	3 M KOH	0 ~ 0.5	132.4 F g^{-1}, 0.5 A g^{-1}	100 % after 10000	[7]
$Co_3(Si_2O_5)_2(OH)_2$	6 M KOH	0.1 ~ 0.55	237 F g^{-1}, 5.7 mA cm^{-2}	95 % after 150	[8]
$Co_3Si_2O_5(OH)_4$	6 M KOH	0 ~ 0.5	570 F g^{-1}, 0.7 A g^{-1}	—	[9]
$MnSiO_3$/GO	1 M Na_2SO_4	-0.2 ~ 1	262.5 F g^{-1}, 0.5 A g^{-1}	53 % after 5000	[10]
$Co_xNi_{3-x}Si_2O_5(OH)_4$	3 M KOH	-0.80 ~ 0.6	226 F g^{-1}, 0.5 A g^{-1}	99 % after 10000	[11]
MnO_2/carbon cloth	0.1 M Na_2SO_4	0 ~ 0.8	230 mF cm^{-2}, 10 mV s^{-1}	98.5 % after 3000	[12]
CoSi hollow sphere	3 M KOH	0 ~ 0.5	452.8 F g^{-1}, 0.5 A g^{-1}	89 % after 10000	[13]
SWCNT/cellulose/PANI	1 M H_2SO_4	-0.2 ~ 0.6	330 mF cm^{-2}, 0.2 mA cm^{-2}	79 % after 1000	[14]
$Zn_4Si_2O_7(OH)_2 \cdot H_2O$	3 M KOH	-1.0 ~ -0.3	517 mF cm^{-2}, 5 mV·s^{-1}	83.4 % after 10000	[15]
ZnO/carbon nanotube	0.1 M TBAPC/DMF	-2 ~ 1	48 F g^{-1}, 1 mA cm^{-2}	95.3 % after 300	[16]
C-ZnSi-N_2	**3 M KOH**	**-1.0 ~ 0.6**	**341 F g^{-1}, 0.5 A g^{-1}**	**99 % after 10000**	**This work**
C-ZnSi-CO_2	**3 M KOH**	**-1.0 ~ 0.4**	**498 F g^{-1}, 0.5 A g^{-1}**	**99 % after 10000**	**This work**

a M = mol L^{-1}

References

[1] J. Zheng, Y. Zhang, Q. Wang, H. Jiang, Y. Liu, T. Lv, C. Meng, Hydrothermal encapsulation of VO_2(A) nanorods in amorphous carbon by carbonization of glucose for energy storage devices, Dalton Trans 47 (2018) 452-464.

[2] Y. Zhang, W. Zhou, H. Yu, T. Feng, Y. Pu, H. Liu, W. Xiao, L. Tian, Self-templated Synthesis of Nickel Silicate Hydroxide/Reduced Graphene Oxide Composite Hollow Microspheres as Highly Stable Supercapacitor Electrode Material, Nanoscale Research Letters 12 (2017) 325.

[3] T. Chen, Z. Shifeng, L. Qingshan, Self-templated synthesis of mesoporous manganese silicates as an electrode material for supercapacitor, Ceramics International 44 (2018) 17007-17012.

[4] H. Wang, Y. Wang, X. Bai, H. Yang, J. Han, N. Lun, Y. Qi, Y. Bai, Manganese silicate drapes as a novel electrode material for supercapacitors, RSC Advances 6 (2016) 105771-105779.

[5] Q. Rong, L. Long, X. Zhang, Y. Huang, H. Yu, Layered cobalt nickel silicate hollow spheres as a highly-stable supercapacitor material, Applied Energy 153 (2015) 63-69.

[6] P. Chaturvedi, A. Kumar, A. Sil, Y. Sharma, Cost effective urea combustion derived mesoporous-Li_2MnSiO_4 as a novel material for supercapacitors, RSC Advances 5 (2015) 25156-25163.

[7] Q. Wang, Y. Zhang, H. Jiang, T. Hu, C. Meng, In Situ Generated $Ni_3Si_2O_5(OH)_4$ on Mesoporous Heteroatom-Enriched Carbon Derived from Natural Bamboo Leaves for High-Performance Supercapacitors, ACS Applied Energy Materials 1 (2018) 3396-3409.

[8] G. Zhang, Y. Zhao, F. Tao, H. Li, Electrochemical characteristics and impedance spectroscopy studies of nano-cobalt silicate hydroxide for supercapacitor, Journal of Power Sources 161 (2006) 723-729.

[9] J. Zhao, Y. Zhang, T. Wang, P. Li, C. Wei, H. Pang, Reed Leaves as a Sustainable Silica Source for 3D Mesoporous Nickel (Cobalt) Silicate Architectures Assembled into Ultrathin Nanoflakes for High-Performance Supercapacitors, Advanced Materials Interfaces 2 (2015) 1400377.

[10] Y. Cheng, Y. Zhang, Q. Wang, C. Meng, Synthesis of amorphous $MnSiO_3$/graphene oxide with excellent electrochemical performance as supercapacitor electrode, Colloids and Surfaces A Physicochemical and Engineering Aspects 562 (2018) 93-100.

[11] Y. Zhang, C. Wang, H. Jiang, Q. Wang, J. Zheng, Cobalt-nickel silicate hydroxide on amorphous carbon derived from bamboo leaves for hybrid supercapacitors, Chemical Engineering Journal 375 (2019) 121938-121938.

[12] Y. Chen, Y. Hsu, Y. Lin, Y. Lin, Y. Horng, L. Chen, K. Chen, Highly flexible supercapacitors with manganese oxide nanosheet/carbon cloth electrode, Electrochimica Acta 56 (2011) 7124-7130.

[13] Q. Wang, Y. Zhang, H. Jiang, X. Li, Y. Cheng, G. Meng, Designed mesoporous hollow sphere architecture metal (Mn, Co, Ni) silicate: A potential electrode material for flexible all solid-state asymmetric supercapacitor, Chemical Engineering Journal 362 (2019) 818-829.

[14] D. Ge, L. Yang, L. Fan, C. Zhang, X. Xiao, Y. Gogotsi, S. Yang, Foldable supercapacitors from triple networks of macroporous cellulose fibers, single-walled carbon nanotubes and polyaniline nanoribbons, Nano Energy 11 (2015) 568-578.

[15] Y. Zhang, H. Jiang, Q. Wang, C. Meng, In-situ hydrothermal growth of $Zn_4Si_2O_7(OH)_2 \cdot H_2O$ anchored on 3D N, S-enriched carbon derived from plant biomass for flexible solid-state asymmetrical supercapacitors, Chemical Engineering Journal 352 (2018) 519-529.

[16] L.S. Aravinda, K.K. Nagaraja, H.S. Nagaraja, K.U. Bhat, B.R. Bhat, ZnO/carbon nanotube nanocomposite for high energy density supercapacitors, Electrochimica Acta 95 (2013) 119-124.